



Article

Titanium Oxyfluoride as a Material for Negative Electrodes of Lithium-Ion Batteries

Ekaterina V. Astrova ^{*}, Vladimir P. Ulin, Alesya V. Parfeneva, Galina V. Li, Maria A. Yagovkina, Darina A. Lozhkina , Andrei A. Krasilin , Maria V. Tomkovich and Aleksander M. Rumyantsev

Ioffe Institute, Russian Academy of Sciences, Politekhnicheskaya st. 26, 194021 Saint Petersburg, Russia

^{*} Correspondence: east@mail.ioffe.ru

Abstract: A study of the electrochemical characteristics of titanium oxyfluoride obtained with the direct interaction of titanium with hydrofluoric acid is reported. Two materials T1 and T2 synthesized under different conditions in which some TiF₃ is formed in T1 are compared. Both materials exhibit conversion-type anode properties. Based on the analysis of the charge–discharge curves of the half-cell, a model is proposed according to which the first electrochemical introduction of lithium occurs in two stages: the first stage is the irreversible reaction resulting in a reduction in Ti^{4+/3+}, and the second stage is the reversible reaction with a change in the charge state Ti^{3+/1.5+}. The difference in material behavior is quantitative: T1 has a higher reversible capacity but lower cycling stability and a slightly higher operating voltage. The Li diffusion coefficient determined from the CVA data for both materials averages 1.2–3.0 × 10^{−14} cm²/s. A distinctive feature of titanium oxyfluoride anodes is the asymmetry in kinetic characteristics that revealed themselves during lithium embedding and extraction. In the long cycling regime, the excess of Coulomb efficiency over 100% was found in the present study.

Keywords: Li-ion batteries; negative electrodes; titanium oxyfluoride; cycling stability; CVA measurements; diffusion coefficient; Coulomb efficiency over 100%



Citation: Astrova, E.V.; Ulin, V.P.; Parfeneva, A.V.; Li, G.V.; Yagovkina, M.A.; Lozhkina, D.A.; Krasilin, A.A.; Tomkovich, M.V.; Rumyantsev, A.M. Titanium Oxyfluoride as a Material for Negative Electrodes of Lithium-Ion Batteries. *Int. J. Mol. Sci.* **2023**, *24*, 4968. <https://doi.org/10.3390/ijms24054968>

Academic Editor: Muhammad Adnan

Received: 12 February 2023

Revised: 1 March 2023

Accepted: 2 March 2023

Published: 4 March 2023



Copyright: © 2023 by the authors. Licensee MDPI, Basel, Switzerland. This article is an open access article distributed under the terms and conditions of the Creative Commons Attribution (CC BY) license (<https://creativecommons.org/licenses/by/4.0/>).

1. Introduction

Transition metal oxides and fluorides have the ability to reversibly absorb lithium during lithium-ion battery operation [1]. A characteristic feature of most of these materials is an irreversible conversion reaction under the first lithiation that results in a partial metal reduction with the release of amorphous Li₂O and/or LiF. Nanoscale precipitates of intermediate compounds containing partially reduced transition metal atoms are formed. Materials undergoing chemical conversion during lithiation/delithiation typically exhibit medium operating voltages (~1 V) and, therefore, can be used both as cathodes [2] and anodes [3–5]. Titanium compounds such as TiF₃ and TiOF₂ have specific capacities exceeding those of carbon, possess high cycling stability and are capable to operate at high currents [3–7]. The latter makes them promising anode materials worthy of detailed study. The main drawbacks of these compounds are relatively low full-cell voltage and low Coulomb efficiency (CE) of the first cycle caused by a conversion reaction and formation of lithium-containing inert products unable to participate in the reversible lithiation/delithiation process. However, the mechanism of electrochemical lithiation of titanium oxyfluoride is still not fully understood, and the drawback related to the initial irreversible losses can probably be overcome by prelithiation [5].

Titanium oxyfluoride, which has semiconductor properties, finds applications in various fields including photocatalysis, UV-absorbing cosmetics, and in LIBs. It should be noted that titanium oxides and fluorides are easily converted from one to the other during the manufacturing process and, therefore, the materials under investigation are often a mixture of several compounds [8,9]. For example, TiOF₂ heating in air leads to the

formation of TiO_2 [4] and, vice versa, fluorination of TiO_2 (anatase) allows the formation of TiOF_2 [5,7,10–12]. Dissolution of metallic titanium in HF in the presence of an oxidizer or, vice versa, in its absence, creates conditions for the formation of TiOF_2 or, correspondingly, TiF_3 . The method of synthesis and the conditions of electrochemical tests strongly influence the value of the specific capacity, which can be reversibly stored by titanium oxyfluoride. Data available in the literature range from 220 to 526 mAh/g [3,5,7,13].

The advantage of titanium oxyfluoride in comparison with other oxides undergoing the conversion reaction during the first lithiation is that the latter proceeds with amorphization of the formed active material and is accompanied by phase separation [5]. Unlike other oxides for which, during the reverse lithium extraction process (oxidation of transition metal), the crystal structure is reduced in the reaction products, for TiOF_2 , such products remain in the amorphous phase. The latter determines a stable value of cycling capacity. The comparatively high operating potential of titanium oxyfluoride relative to lithium makes it possible to expect that lithiation at low temperatures will occur without the deposition of metallic Li, as well as in the case of lithium titanate. All this makes TiOF_2 promising for applications as LIB anodes. Unlike other titanium compounds TiO_2 and $\text{Li}_4\text{Ti}_5\text{O}_{12}$ (LTO), the electrochemical characteristics of titanium oxyfluoride are poorly understood, and the present study aims to fill this gap.

2. Results and Discussion

2.1. Galvanostatic Tests

The electrodes were fabricated using the “slurry” technology. For this purpose, titanium oxyfluoride powders were rubbed in an agate mortar and mixed with dry components in the weight ratio T1 (or T2): carbon black: VGCF (vapor grown carbon fibers, Showa Denko) = 88%: 5%: 2%, to which a binder solution consisting of N-methylpyrrolidone and polyvinylidene fluoride (PVDF) Solef 5130 (Solvay, Shanghai, China) was then added in a 17:1 ratio. Electrodes 15 mm in diameter were mounted in CR2032 disc cells with a lithium counter electrode and Celgard 2325 as a separator. The electrolyte used was TC-E918 (Tinci), which is a 1M solution of LiPF_6 in an EC/PC/DEC/EMC/PA mixture (ethylene carbonate, propylene carbonate, diethyl carbonate, ethyl methyl carbonate, propyl acetate).

Charge–discharge curves of T1-Li (or T2-Li) half-cells were recorded in galvanostatic mode using a CT3008W-5V10mA (Neware, Shenzhen, China) cycle tester. During Li embedding (charging), the voltage across the test electrodes was limited to 10 mV, and during Li extraction (discharging), it was limited to $U = 3$ V. The long-term tests, the results of which are shown in Figures 1–4a, started with the first three cycles ($N = 1$ –3) of charge–discharge being carried out at current density $j = 30$ mA/g, then three cycles ($N = 4$ –6) at $j = 100$ mA/g, and another three cycles ($N = 7$ –9) at $j = 200$ mA/g. Further tests were performed at $j = 100$ mA/g. Cycling at $j = 400$ mA/g, presented in Figure 4b, followed the initial 12 cycles at $j = 30$ –800 mA/g (see Figure 5a). The cycling was carried out without the cell being thermostatted.

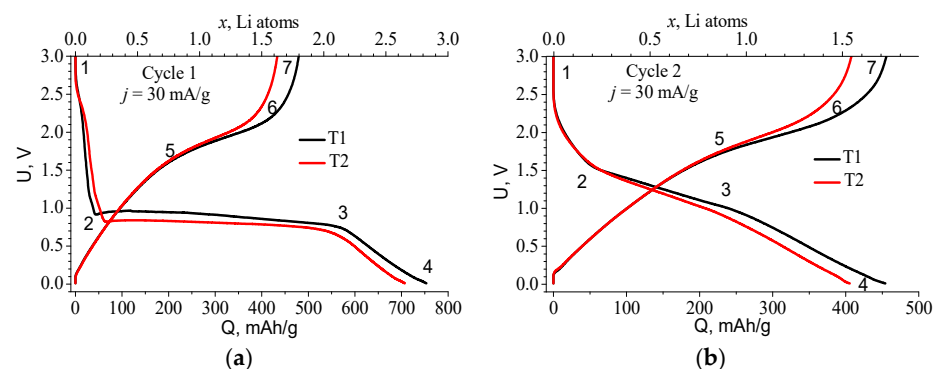


Figure 1. Charge–discharge curves of the T1 and T2 anodes: (a) first and (b) second cycle, recorded at $j = 30$ mA/g.

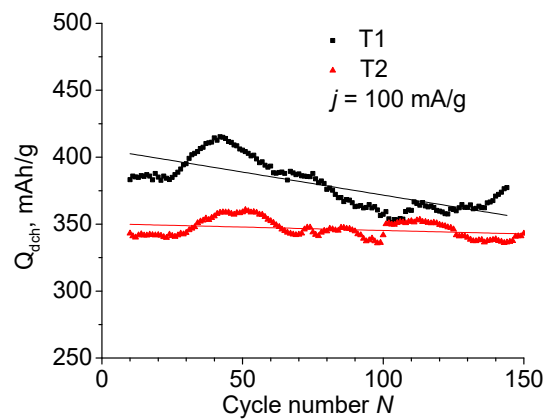


Figure 2. Discharge capacity of T1 and T2 anodes as a function of cycle number.

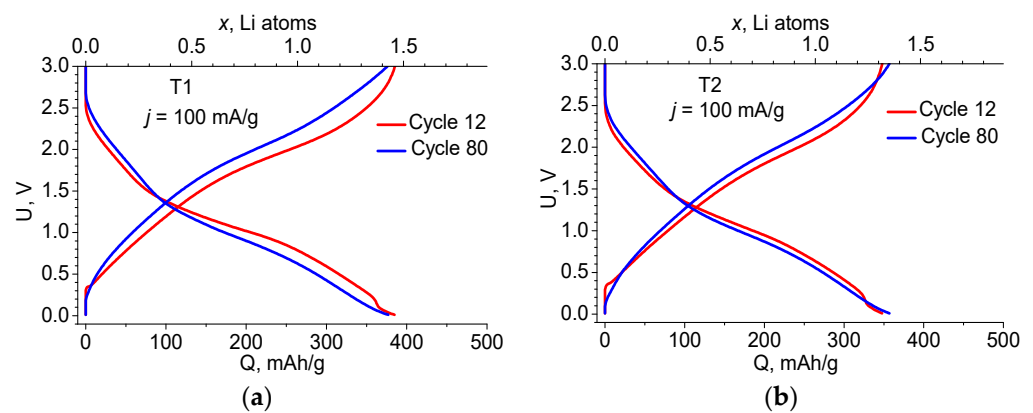


Figure 3. Charge–discharge curves of the 12th and 80th cycles at $j = 100 \text{ mA/g}$ for the T1 (a) and T2 (b) anodes.

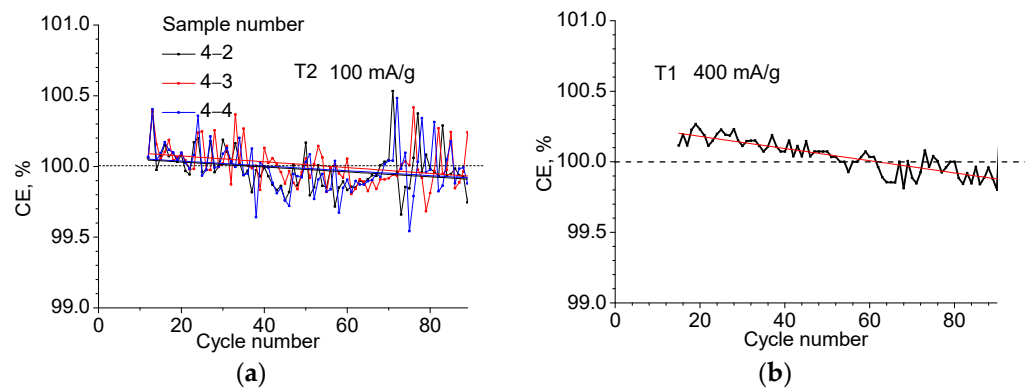


Figure 4. Coulombic efficiency of three T2 samples at current density $j = 100 \text{ mA/g}$ (a) and one T1 sample at $j = 400 \text{ mA/g}$ (b) as a function of cycle number.

The charge curve for the first lithiation is fundamentally different from subsequent cycles (Figure 1). It has a long horizontal plateau which is characteristic of the materials forming two phases during lithiation. The position of this plateau is slightly different for the two materials: in the case of T1, it is higher with an average value of 0.82 V, and in the case of T2, with an average value of 0.74 V. Table 1 makes it possible to estimate the number of lithium g-atoms embedded in the different sections of the curve. The formula $x = Q \cdot M / F = 3.8 \times 10^{-3} \cdot Q$, where M is the molar mass of $\text{TiOF}_2 = 101.88 \text{ g/mol}$, Q in mAh/g , and $F = 26,801 \text{ mAh/mol}$, was used for the calculation of lithium g-atoms number x per TiOF_2 mole.

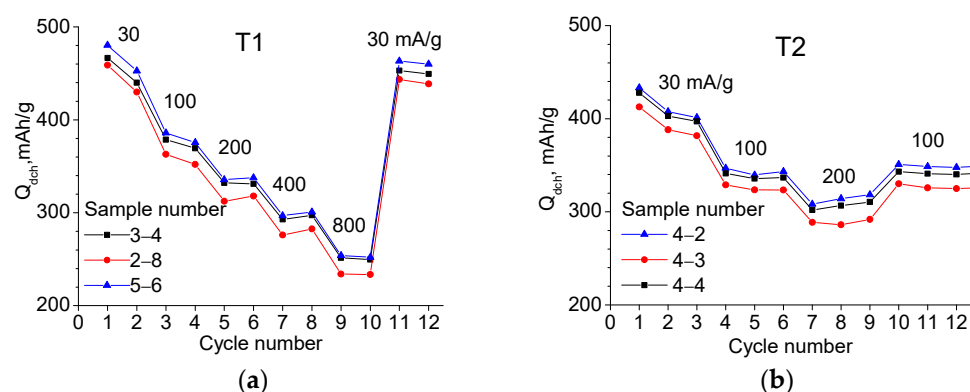


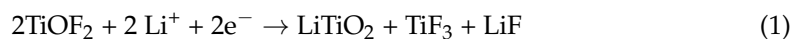
Figure 5. Dependencies of the discharge capacity on cycle number obtained with different charge–discharge currents shown in the figure: (a) for T1 and (b) for T2 materials (three samples of each).

Table 1. Coordinates of characteristic points on charge and discharge curves of cycle 1 (Figure 1a), their corresponding amount of embedded or extracted lithium x , and its increment Δx at each step.

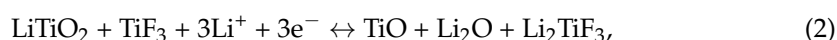
Point	U, V		$Q, mAh/g$		$x Li$		Range	Δx	
	T1	T2	T1	T2	T1	T2		T1	T2
1	3	3	0	0	0	0			
2	0.91	0.82	42.8	62.5	0.16	0.24	1–2	0.16	0.24
3	0.73	0.66	574	557	2.17	2.11	2–3	2.01	1.87
4	0.01	0.01	753	706	2.85	2.67	3–4	0.68	0.56
5	1.69	1.62	227	199	0.86	0.76	4–5	2.23	1.91
6	2.35	2.31	442	396	1.68	1.50	5–6	0.82	0.74
7	3	3	477	432	1.81	1.64	6–7	0.13	0.14

The structure change in $TiOF_2$ as a result of electrochemical lithiation at its different stages was studied in [3,5] using X-ray diffraction (XRD), X-ray photoelectron spectroscopy (XPS), and X-ray absorption near-edge structure (XANES). According to Table 1, 0.16 and 0.24 Li atoms, respectively, are first introduced into the T1 and T2 material at voltages above the plateau. Under this stage, the structure of the material remains crystalline.

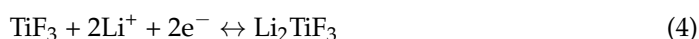
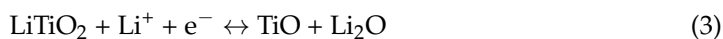
In the plateau region (range 2–3), the introduction of ~ 2 lithium g-atoms occurs. It is accompanied by the formation of LiF, partial reduction of Ti, and amorphization of the material [3,5]. The last lithiation range 3–4 corresponds to the introduction of Li into the amorphous phase. The maximum amount of lithium introduced during the first lithiation is 2.85 and 2.67 g-atoms for T1 and T2 materials, respectively. It can be assumed that the first lithium introduction results in a conversion reaction resulting in the formation of several compounds. It may correspond to an irreversible reaction involving 2 Li ions:



where the oxidation state of titanium changes from 4+ to 3+. Further lithiation of titanium compounds can continue with the participation of 3 Li ions, but this time reversibly:



which suggests two independent reactions:



The total reaction (1) and (2), corresponding to the first introduction of lithium, can be represented as:



Thus, 1 mole of titanium oxyfluoride in our supposed scheme of sequential lithiation absorbs $5/2 = 2.5$ lithium atom, which is in good agreement with the data in Table 1. In this case, lithium fluoride is considered to be inert, and the formation of free titanium (Ti^0) does not occur, which corresponds to the data of [3,5]. The irreversible reaction (conversion reaction) during the first introduction of lithium into TiOF_2 strongly reduces the Coulomb efficiency (CE) of the first cycle. For T1 and T2 materials, it is 63% and 60%, respectively. According to reactions (1)–(5), the irreversible losses of the first cycle are $2/5 = 0.4$, which agrees well with the experimental values of CE. Thus, the electrochemical characteristics of both materials are extremely similar, differing only in the voltage at which the plateau appears and the value of the introduced/removed charge.

Figure 1b shows the S-curves of cycle 2, the characteristic points of these curves are given in Table 2. Starting from the second cycle a reversible redox reaction identical to the second stage of the first lithiation (2) takes place. During the lithiation, titanium is reduced to Ti^{2+} in TiO (3) and to Ti^+ in Li_2TiF_3 (4), which corresponds to an average valence value of $\text{Ti}^{1.5+}$. Hence, there are 3 Li atoms per 2 Ti atoms, i.e., Li/Ti ratio $x = 1.5$, which corresponds to a theoretical capacity of 395 mAh/g. This value is slightly lower than the total absorbed lithium $x = 1.54$ for T2 material (see Table 2) found from experiments. For T1, this value is even greater: $x = 1.72$, which can be explained by a higher content of TiF_3 . TiF_3 can reversibly absorb 3 lithium atoms (its theoretical capacity 766.6 mAh/g) [1]. Thus, at the end of the Li embedding process, titanium is reduced to $\text{Ti}^{1.5+}$ on average, and by the end of lithium extraction, it is oxidized to Ti^{3+} . The latter is in agreement with the data of [3], which holds that the charge state of Ti decreases to values <3 during reversible lithiation, but differs from the conclusions of [5], according to which $\text{Ti}^{2+/4+}$ reduction/oxidation occurs during lithium embedding/extraction. Since in our experiments for both materials the reversible capacity Q_{exp} was higher than that calculated for TiOF_2 (within the proposed model), this discrepancy allows us to estimate the amount of TiF_3 in each material using a simple equation:

$$766.6y + 395(1 - y) = Q_{\text{exp}} \quad (6)$$

where y is the mass fraction of TiF_3 . Such an estimation gives for T1 material $y = 15.9\%$, and for T2, $y = 2.7\%$.

Table 2. Potential and amount of lithium introduced or extracted for the characteristic points on the charge and discharge curves of cycle 2 (Figure 1b) and their corresponding x and increment Δx at each interval between these points.

Point	U, V		$Q, \text{mAh/g}$		$x \text{ Li}$		Range	Δx	
	T1	T2	T1	T2	T1	T2		T1	T2
1	3	3	0	0	0	0			
2	1.55	1.55	52.5	56.0	0.20	0.21	1–2	0.20	0.21
3	1.01	0.96	236	220	0.89	0.83	2–3	0.69	0.62
4	0.01	0.01	454	405	1.72	1.54	3–4	0.83	0.71
5	1.79	1.69	247	221	0.94	0.84	4–5	0.78	0.70
6	2.38	2.15	414	337	1.57	1.28	5–6	0.63	0.44
7	3	3	455	407	1.73	1.55	6–7	0.16	0.27

2.2. Cycle Life

After the first nine cycles, the anodes T1 and T2 were tested at a constant current of $j = 100 \text{ mA/g}$. Figure 2 shows the dependence of the discharge capacity on the number of charge–discharge cycles N . The observed fluctuations are due to temperature changes in the room where the tests were carried out. After ~ 100 – 140 cycles, the lithium counter-electrode degrades, which appears as a capacity drop. Replacing the lithium in the cell returns the Q_{ch} and Q_{dch} to their previous values. Fitting of the curves with linear dependence is

expressed using the formulas $Q_{\text{dch}}(\text{T1}) = 406 - 0.344N$ and $Q_{\text{dch}}(\text{T2}) = 350 - 0.051N$, i.e., the specific capacity of T1 material containing TiF_3 is higher than of T2, but the degradation rate is noticeably higher, too.

Figure 3 shows how the charge–discharge curves change from cycle 12 to cycle 80 for both materials. The changes are small and are most likely due to the increase in the electrical resistance of the materials.

The Coulomb efficiency behaves somewhat unusually. From Figure 1b and Table 2, it can be seen that in the second cycle, the amount of electricity extracted exceeds the amount injected by 0.26 and 0.51% for the T1 and T2 materials, respectively, and the Coulomb efficiency appears to be >100%. Figure 4a shows the CE fluctuations occurring after the 12th cycle up to $N = 90$ when tested at constant charge/discharge current value $j = 100 \text{ mA/g}$, and in Figure 4b, at $j = 400 \text{ mA/g}$. Approximating the dependencies with a linear function and averaging over the samples indicates a slowly decreasing dependence with a slope of 0.002% per cycle for $j = 100 \text{ mA/g}$ and a slope of 0.004% for $j = 400 \text{ mA/g}$. The crossing of the 100% boundary occurs between 40 and 60 cycles. It can be assumed that in this region, the degradation starts to override the effect of additional lithium release. The behavior of the Coulomb efficiency during long cycling in the galvanostatic regime seems to be a result of the fact that one of the lithium compounds formed in the conversion reaction during the first introduction of lithium (in this case LiF) does not remain completely inert and turns out to be able to contribute to the lithium yield during the reverse electrochemical reaction. The electrochemical decomposition of LiF and Li_2O is known to be activated with the participation of transition metals or their oxides [14]. The gradual depletion of an additional source of Li occurs slowly but serves to cause the observed phenomenon where the observed CE exceeds 100% by 0.1–0.2% over several tens of cycles.

2.3. Power Characteristics

To investigate the charge–discharge current dependence Q_{dch} , three samples from each material were used, which showed good reproducibility (see Figure 5). In the case of T1, the current was varied from 30 to 800 mA/g—two cycles at each current. In the case of T2, the current varied from 30 to 200 mA/g—three cycles each. In both cases, increasing the current from 30 to 200 mA/g results in a capacity reduction of 1.35 times.

2.4. Cyclic Voltammetry (CVA)

The measurements were carried out on a Biologic VSP modular potentiostat/galvanostat. Experiment E1 used samples that had previously undergone two cycles. In this way, the third cycle dependencies were recorded when the voltages were sweeping at different speeds (0.05–2 mV/s). In experiment E2, the sweep rate was $v = 0.2 \text{ mV/s}$ starting from cycle 1. In experiments E3 and E4, both materials were investigated, and the sweep speed $v = 0.05 \text{ mV/s}$. These experiments make it possible to compare the electrochemical properties of T1 and T2 materials and also to determine Li diffusion coefficients in each material. Table 3 shows the details of the experiments and the parameters of the samples. The surface area S of the samples was calculated from the average particle size a in the starting material $S = 6m/(\rho \cdot a)$; in both cases $a = 1 \mu\text{m}$ (SEM data in figure in Section 3.2, SEM images).

Table 3. Conditions of experiments and parameters of anodes in the CVA measurement.

Experiment	Sweep Speed v , mV/s	Cycle Number	Material	m , mg	ρ , g/cm ³	S , cm ²
E1	0.05–2	3–9	T1	7.74	2.79	166
E2	0.2	1–11	T1	7.66	2.79	165
E3	0.05	1–2	T1	7.48	2.79	161
E4	0.05	1–2	T2	6.95	3.07	136

The results of experiment E1 are shown in Figure 6 and Table 4.

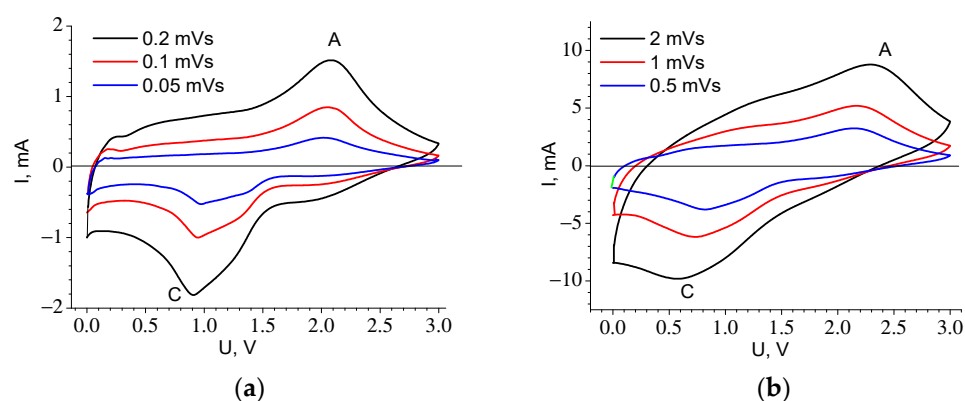


Figure 6. CVA recorded at different sweep speeds in T1 material (experiment E1): (a) $v = 0.05\text{--}0.2$ mV/s, (b) $v = 0.5\text{--}2$ mV/s.

Table 4. Voltage position of C and A peaks (T1 3rd cycle).

v , mV/s	Peak Position Cathode, V	Peak Position Anode, V
0	0.976	2.03
0.05	0.966	2.02
0.1	0.948	2.06
0.2	0.907	2.08
0.5	0.819	2.14
1	0.722	2.17
2	0.568	2.28

One cathodic C and one anodic A peak are well pronounced. Their position is consistent with the flattest parts of the charge–discharge curves (see Figures 1b and 3, Table 2). As the sweep speed increases, the peaks move apart in voltage from each other and become blurred.

Figure 7 shows the dependencies of their respective voltage on v . The position of the peaks for $v = 0$ mV/s in Table 4 is obtained using extrapolation of the curves. It can be seen that the dependencies are nonlinear, which makes it impossible to explain the shift solely by the contribution of series ohmic resistance. The cathode peak is more sensitive to the sweep speed than the anode peak: the former is shifted in voltage by 0.41 V and the latter by 0.25 V. This result indicates the asymmetry of the kinetic properties during charging and discharging. Figure 8 shows the dependence of the height of the anode (A) and cathode (C) peaks on the square root of the voltage sweep rate. Its linearity indicates that the main process limiting the charge and discharge rate is diffusion [15].

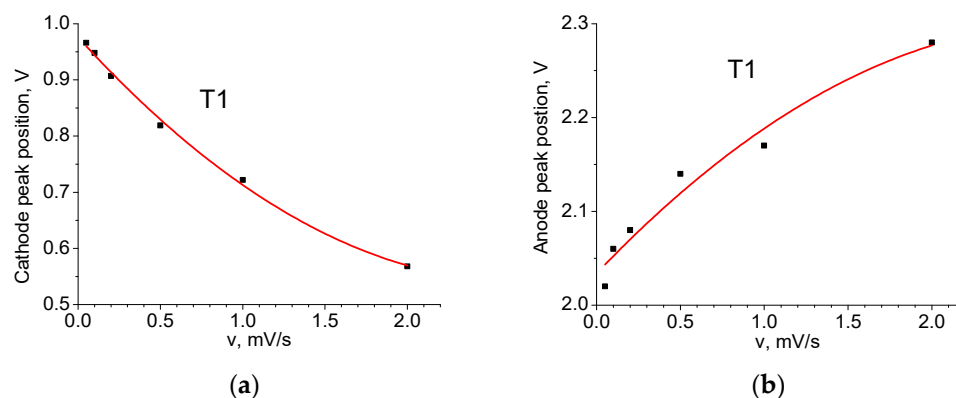


Figure 7. Position of voltage peaks as a function of sweep speed (T1 material): (a) cathode C; (b) anode A.

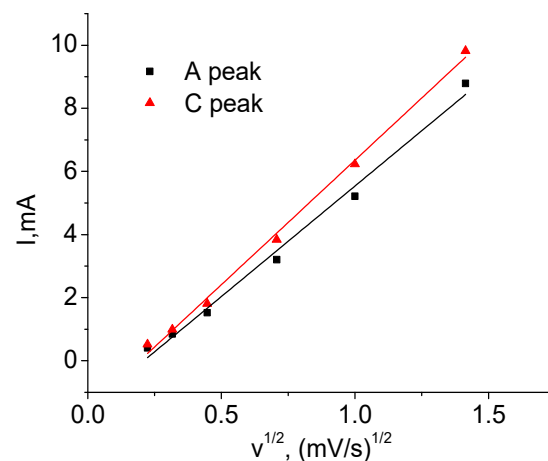


Figure 8. Height of the cathode and anode peaks as a function of voltage sweep speed (T1).

Figure 9 shows the results of experiment two—the dependence on the number of cycles. In Figure 9b, from the intermediate cycles between the second and eleventh one, it can be seen that as the number of cycles increases, the relative height of peaks 0.88 and 1.03 is changed. This corresponds to a decrease in height of the cathode peak 1.03 with its simultaneous shift towards higher voltages so that by cycle 5, it looks like a small shoulder. At the same time, the 0.88 cathode peak and the 2 V anode peak just slightly change their voltage position. With an increasing number of cycles, an additional 0.6 V anode peak and 2.02 V cathode peak appear.

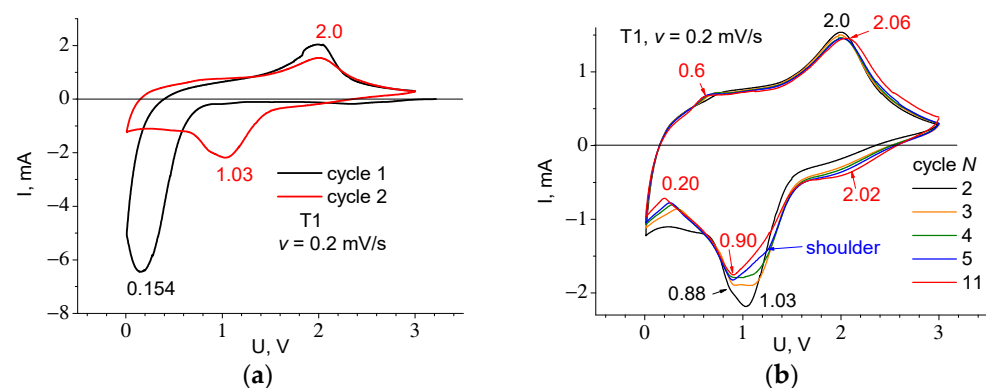


Figure 9. CVA curves recorded at sweep rate $v = 0.2$ mV/s for cycles: (a) 1 and 2 and (b) for 2 and 11. Cycle 2 in figures (a,b) are shown at different scales for easy comparison with other cycles.

Figure 10 shows the CVA of cycle 1 and cycle 2 recorded at low speed (experiments E3 and E4), and Table 5 shows the parameters of the observed peaks. The difference between the T1 and T2 materials is present only in the first cycle where the 1C cathode peak for T1 is located at a higher voltage than for T2, the same as the plateau in the first charging curve. The presence of two peaks on the cathodic part of the curve for cycle 2 can testify to the Li introduction mechanism corresponding to the formation of different compounds Li_2O and Li_2TiF_3 , (see Equations (3) and (4)). Both T1 and T2 materials exhibit significant hysteresis, which is clearly visible from the difference in voltages for the anodic and cathodic peaks (Figure 10b) and from the voltage location of the gentle sections 2–3 and 5–6 on the charge and discharge curves (Figure 1b and Table 2). In addition to the polarization component, its presence is most likely due to the so-called path hysteresis [16].

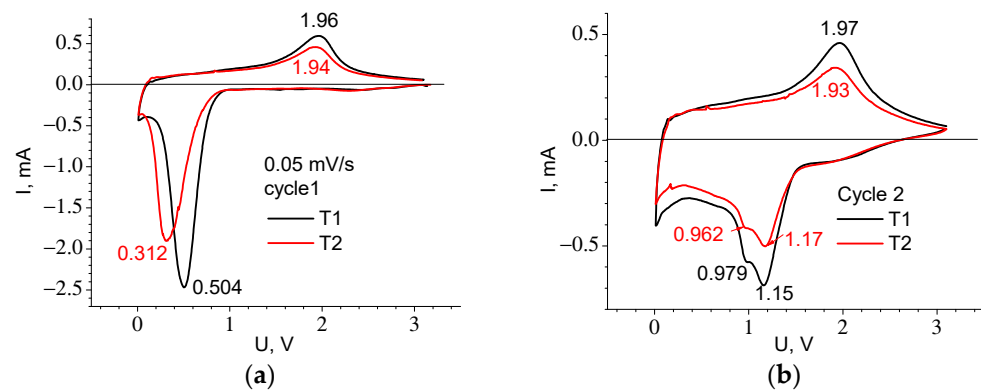


Figure 10. CVA curves recorded at the sweep speed $v = 0.05$ mV/s for cycle 1 (a) and cycle 2 (b).

Table 5. Parameters and designations of CVA peaks for samples T1 and T2 obtained at sweep speed $v = 0.05$ mV/s.

1 Cycle					2 Cycle				
T1		T2		Peak Designation	T1		T2		Peak Designation
U, V	I, mA	U, V	I, mA		U, V	I, mA	U, V	I, mA	
0.504	−2.46	0.312	−1.9	1C	1.15	−0.684	1.17	−0.500	3C
1.96	+0.598	1.94	+0.461	2A	0.979	−0.576	0.962	−0.414	4C
					1.97	+0.459	1.926	+0.341	5A

2.5. Determination of the Diffusion Coefficient

The mean value of diffusion coefficient D of lithium in the electrode material was determined using the height of CVA peaks of the dependences recorded at low speed in experiments E3 and E4 separately for the cathode and anode half-cycle. For this purpose, the Randles–Shevcik equation was applied [17,18]:

$$I_p = 2.69 \times 10^5 S c_0 (z D v)^{1/2} \quad (7)$$

where c_0 is the maximum concentration of lithium embedded in or extracted from the electrode in mol/cm³, S is the inner surface area [cm²], v is the voltage sweep rate [V/s], I_p is the peak current [A]. The dimension of the coefficient is 2.69×10^5 [A·s·mol^{−1}·V^{−1}], and z is an empirical fitting parameter. Equation (7) was derived from a modified Nernst equation [15] defining the relation between the electrode potential and concentration of potential-determining particles and taking into account the difference between the concentration and activity of diffusing particles:

$$E = E_0 - (RT/znF) \ln c \quad (8)$$

The necessity to introduce the fitting parameter z is due to the fact that the equilibrium dependence of potential E on c in the general case does not obey the Nernst equation. At room temperature, $RT/F = 2.57 \times 10^{-2}$ V, number of electrons $n = 1$, and therefore (8) appears as:

$$E = E_0 - 2.57 \times 10^{-2} \ln c z^{-1} \quad (9)$$

Thus, comparing the slope s of the empirical relationship $E = f(\ln c)$ with the slope of relationship (9) we can determine $z = 2.57 \times 10^{-2} / |s|$. The relation between the lithium concentration [mol/cm³] and the amount of electricity Q [C] present in the electrode is determined using the formula:

$$c = Q \cdot \rho / m \cdot F \quad (10)$$

where ρ [g/cm³] and m [g] are the density and mass of the active component of the electrode, respectively, and the Faraday constant $F = 9.65 \times 10^4$ C/mol.

Let us first determine D for the T1 material from CVA cycle 2 based on the height of cathode peak 3C $I_p = -0.684$ mA (see Table 5). To find c_0 , we used the maximum charge accumulated at the cathode half-cycle, $Q_{\max C} = 12.94$ C, which was obtained by integrating the dependence $I = f(t)$. The corresponding value was $c_0 = 0.050$ mol/cm³. From the slope of the straight line in Figure 11a, we determined $z = 0.066$. Taking into account electrode surface area $S = 161$ cm² from (7), we find $D = 3.02 \times 10^{-14}$ cm²/s.

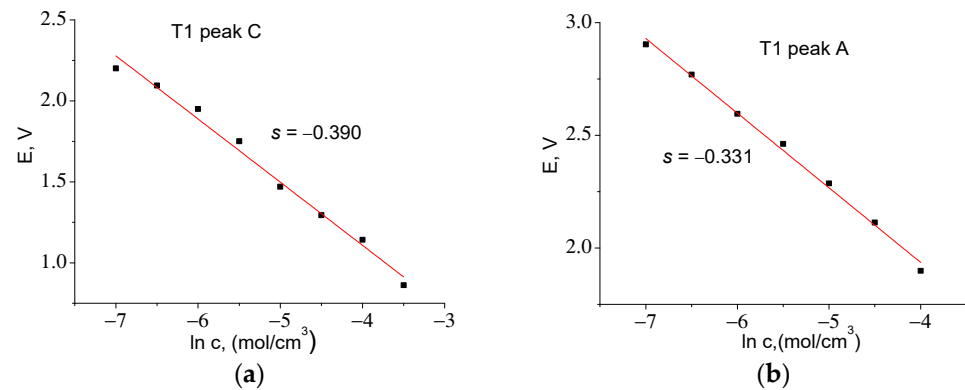


Figure 11. Experimental dependences of $E = f(\ln c)$ for T1 series samples for: (a) cathodic ($z = 0.066$) and (b) anodic ($z = 0.078$) parts of CVA.

By integrating $I = f(t)$ in the anode part of the CVA, it was found that $Q_{\max A} = 12.43$ C, $c_0 = 0.048$ mol/cm³. The slope $E = f(\ln c)$ $s = -0.331$, whence $z = 0.078$ and $D = 1.24 \times 10^{-14}$ cm²/s. A similar procedure for the T2 material (Figure 12) made it possible to find the correction factor z and to calculate the diffusion coefficients for the cathode and anode peaks. Table 6 shows that the diffusion coefficients found for both materials are almost the same.

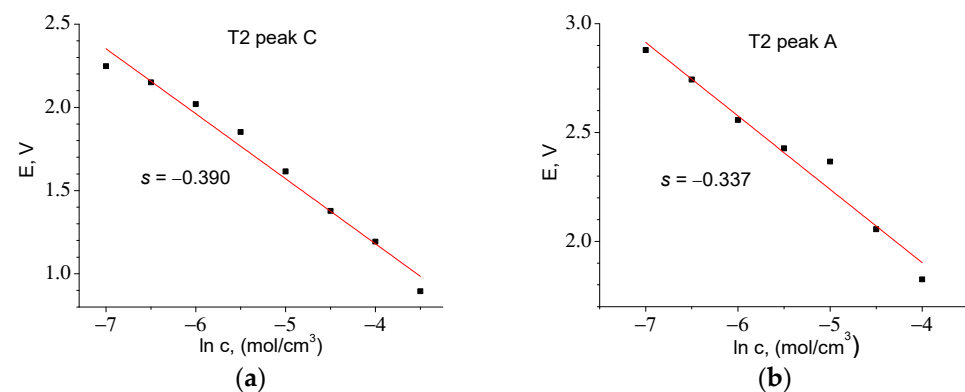


Figure 12. Experimental dependences of $E = f(\ln c)$ for T2 series samples: (a) for cathodic ($z = 0.066$) and (b) for anodic ($z = 0.076$) parts of CVA.

Table 6. Diffusion coefficient values for T1 and T2 electrodes (second cycle $v = 0.05$ mV/s).

	T1		T2	
	from Peak 3C	from Peak 5A	from Peak 3C	from Peak 5A
$D, \text{cm}^2/\text{s}$	3.02×10^{-14}	1.24×10^{-14}	2.78×10^{-14}	1.26×10^{-14}

The obtained D values are rather low. The low Li diffusion coefficient leads to a high polarization, i.e., a large deviation in the charge and discharge dependences from the equilibrium curves. As a result, Li insertion takes place at lower potentials relative to lithium, and extraction, respectively, at higher ones. Thus, with an increase in the current, a

significant reduction in capacity occurs both for Li insertion and extraction. The effect of current on the discharge capacity can be seen in Figure 5.

3. Materials and Methods

3.1. Synthesis

The starting material was obtained using direct interaction of titanium in the air with hydrofluoric acid (48–49% HF solution in water). The condition of solid-state oxyfluoride deposition is a constant contact of titanium with the solution in which HF deficiency occurs. The reaction of titanium with hydrofluoric acid begins with the evolution of hydrogen and TiF_4 , which forms with HF in an aqueous solution a colorless fluorotitanic acid (H_2TiF_6). This heterogeneous reaction is exothermic and accelerates as the components heat up. At the same time, the degree of oxidation of titanium at the reaction interphase begins to decrease, apparently, due to the participation of the primary product, H_2TiF_6 , in the further interaction. Then, along with TiF_4 , TiF_3 is released into the HF solution giving brown-colored acid H_2TiF_5 . As HF is exhausted, the dissociation of formed acids begins with the detachment of HF and hydrolysis of titanium tetrafluoride: $\text{TiF}_4 + \text{H}_2\text{O} = \text{TiOF}_2 + 2\text{HF}$. TiF_3 , which is not inclined to hydrolysis, remains in the precipitate together with the released titanium oxyfluoride. When the reaction is carried out in the air, there is a possibility of gradual oxidation of finely dispersed TiF_3 by dissolved oxygen with the formation of tetravalent titanium oxyfluoride: $4\text{TiF}_3 + \text{O}_2 + 2\text{H}_2\text{O} = 4\text{TiOF}_2 + 4\text{HF}$. Therefore, without restricting air access and creating conditions for continuous close contact of titanium with HF-containing solution, it is difficult to achieve a high concentration of TiF_3 in the resulting precipitate.

Under T1 synthesizing, when the aim was to obtain an appreciable amount of TiF_3 in the reaction product, the process was carried out in a titanium beaker filled with small pieces of titanium and having a lid. Hydrofluoric acid was introduced in small portions with interruptions to stop active interaction with outgassing. After repeated stirring, until the visible hydrogen evolution ceased, followed by a three-hour exposure time, ethyl alcohol was poured into the beaker, and the reaction products were separated from the remaining titanium. Drying was carried out under low heat. For T2 synthesis, the reaction was carried out in an open PTFE beaker, and the products were flooded with water and separated from the excess titanium. The drying of the powder was carried out at ~70–80 °C.

3.2. Physicochemical Characteristics

The obtained weakly colored powders were subjected to X-ray phase analysis (XRD). Registration of diffraction curves was carried out on X-ray diffractometer D2PHSER firm Bruker AXS (Karlsruhe, Germany) equipped with a sharp-focus X-ray tube with a copper anode ($\lambda\text{-k}_{\alpha 1} = 1.50056 \text{ \AA}$, $\text{k}_{\alpha 2} = 1.54439 \text{ \AA}$), PSD-detector Lynxeye. Registration of the reflected signal intensity was performed in the angle range of 10–85 degrees on the 2θ scale, the registration step was 0.02 degrees, and the signal accumulation time at the point was 1 s. Analysis of the obtained curves was carried out with the Bruker DIFFRAC.EVA V4.1.1 software package. Diffractograms were interpreted based on the ICDD database, release 2014, PDF2. The XRD results and comparison with tabulated data are shown in Figure 13.

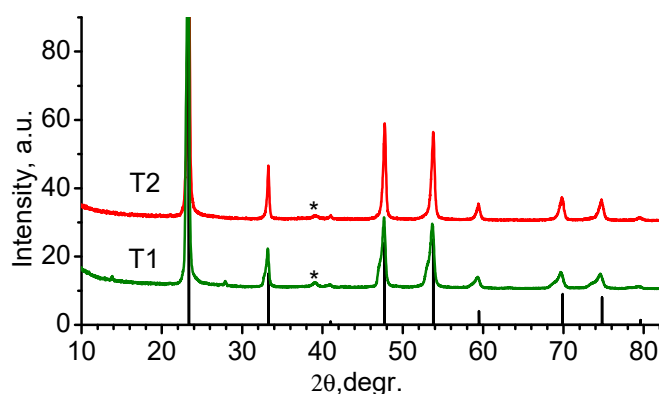


Figure 13. Diffraction curves from materials obtained with T1 and T2 synthesis; the line bar diagram corresponds to the positions and relative intensities of TiOF_2 diffraction maxima PDF-01-076-7831; * peak of the most intense TiO_2 reflex (rutile).

The decoding of the diffractogram of the T2 sample showed that the main phase is the cubic modification of TiOF_2 of space group $\text{Pm}\bar{3}\text{m}$. An insignificant TiO_2 (rutile) admixture is also visible in the sample. In sample T1, the rutile admixture is also present, and the main phase is titanium oxyfluoride. However, the curve (Figure 13, T1) shows an asymmetric shape of all TiOF_2 diffraction peaks, and the reflexes have a “shoulder” at the lower 2θ angles. This picture can be explained by the formation of an additional phase with a structure similar to titanium oxyfluoride but with a larger unit cell parameter. The lattice parameter difference between TiOF_2 and the additional phase is 0.082 nm. This probably indicates the beginning of restructuring from TiOF_2 to TiF_3 .

Electron microscopic studies and X-ray spectral microanalysis (EDX) of the obtained materials were carried out using an FEI Quanta 200 scanning electron microscope with an EDAX energy-dispersive microanalyzer. Figure 14 shows images of T1 and T2 powders, and Table 7 shows their composition. The structure of the powders can be characterized as fine-crystalline with particles ~1 μm in size, on which faceting elements are visible.

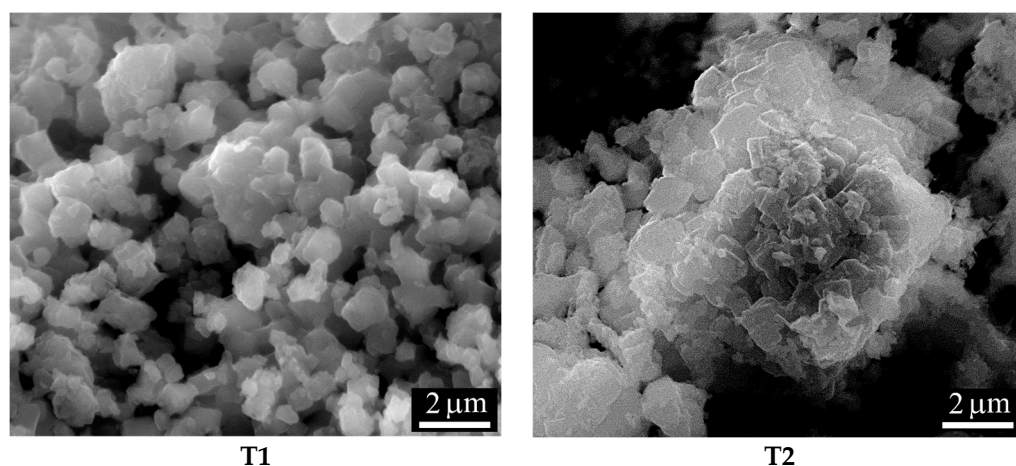


Figure 14. SEM images of the synthesized powders.

The true (pycnometric) density of obtained powders was measured with gas (helium) pycnometry on an Ultrapycnometer 1000 device of Quantachrome Company (Boynton Beach, FL, USA). Table 7 shows the density of powders and their elemental composition. The latter was measured in 5 points for each powder, and the table shows average values.

It follows from the data in Table 7 that the average oxidation degree of Ti in material T1 is lower than in T2. Since the valence of Ti in the oxyfluoride must be 4, its lowering indicates a higher proportion of 3-valent titanium (TiF_3) in the T1 material. These results are in qualitative agreement with XRD data.

Table 7. Pycnometric density, the elemental composition of materials, and average oxidation degree of Ti in the studied materials T1 and T2.

	T1		T2	
Density ρ , g/cm ³	2.79		3.07	
Element	At%	Value reduced to Ti	At%	Value reduced to Ti
Ti	25.3	1	23.9	1
O	22.6	0.89	22.6	0.94
F	52.6	2.08	53.5	2.24
Ti averaged oxidation degree	3.86		4.12	

4. Conclusions

Titanium oxyfluoride was obtained using the interaction of metallic Ti with hydrofluoric acid in a deficiency of the latter. The initial oxidation degree of titanium in the investigated products T1 and T2, formed under somewhat different conditions of reagent contact with air, was not identical. In T1, it is markedly lower than four, which is due to the presence of a larger amount of TiF₃. The latter is in agreement with XRD data and the higher value of specific capacity of the anode.

According to the proposed model, the conversion reaction of TiOF₂ during the first lithiation consists of irreversible and reversible parts. The former proceeds with the formation of LiTiO₂, TiF₃, and LiF, resulting in the reduction of titanium to Ti³⁺. The reversible redox reaction proceeds with the formation of TiO, Li₂O, and Li₂TiF₃ as final reduction products and with a change in the average charge state of titanium Ti^{3+/1.5+}, which corresponds to the introduction and extraction of 1.5 g-atom of lithium per 1 g-mole of TiOF₂.

CVA studies allowed for the first time to determine the Li diffusion coefficient in titanium oxyfluoride electrodes $D = 1.2\text{--}3.0 \times 10^{-14} \text{ cm}^2/\text{s}$.

The Coulomb efficiency of TiOF₂ electrodes in the first cycle is low 60–63%, but in the subsequent ones, it is close to 100%. In addition, an unusual behavior of the Coulomb efficiency of TiOF₂ exceeding 100% at cycling was revealed. The latter allows us to assume that LiF separated with the first lithiation does not remain completely inert in the subsequent delithiation processes.

Titanium oxyfluoride shows high stability in the cycling tests. During 100 cycles at a current of 100 mA/g (C/4), the T1 material retains a Q_{dch} higher than the theoretical value for the carbon anode. Both the T1 and T2 materials have a capacity higher than other titanium-based anodes such as TiO₂ and LTO. T2 shows the highest degradation resistance: its discharge capacity of 345 mAh/g ($j = 100 \text{ mA/g}$) practically does not change within 150 cycles.

The disadvantages of the synthesized materials are significant voltage hysteresis, which must lead to energy loss due to heat dissipation, and low Coulomb efficiency of the first cycle.

Author Contributions: Conceptualization: V.P.U., A.M.R., and E.V.A.; methodology: V.P.U. and A.M.R.; formal analysis: A.V.P. and G.V.L.; investigation: A.M.R., A.V.P., G.V.L., M.A.Y., D.A.L., A.A.K., and M.V.T.; resources: A.M.R.; data curation: E.V.A.; writing—original draft preparation: E.V.A.; writing—review and editing: V.P.U., A.M.R., and A.V.P. supervision: E.V.A.; project administration: E.V.A. All authors have read and agreed to the published version of the manuscript.

Funding: This research was funded by the State Task 0040-2019-0012.

Institutional Review Board Statement: Not applicable.

Informed Consent Statement: Not applicable.

Data Availability Statement: Not applicable.

Conflicts of Interest: The authors declare no conflict of interest.

References

1. Li, H.; Balaya, P.; Maier, J. Li-Storage via Heterogeneous Reaction in Selected Binary Metal Fluorides and Oxides. *J. Electrochem. Soc.* **2004**, *151*, A1878–A1885. [[CrossRef](#)]
2. Kitajou, A.; Eguchi, K.; Ishado, Y.; Setoyama, H.; Okajima, T.; Okada, S. Electrochemical properties of titanium fluoride with high rate capability for lithium-ion batteries. *J. Power Sources* **2019**, *419*, 1–5. [[CrossRef](#)]
3. Reddy, M.; Madhavi, S.; Rao, G.S.; Chowdari, B. Metal oxyfluorides TiOF₂ and NbO₂F as anodes for Li-ion batteries. *J. Power Sources* **2006**, *162*, 1312–1321. [[CrossRef](#)]
4. Chen, L.; Shen, L.; Nie, P.; Zhang, X.; Li, H. Facile hydrothermal synthesis of single crystalline TiOF₂ nanocubes and their phase transitions to TiO₂ hollow nanocages as anode materials for lithium-ion battery. *Electrochim. Acta* **2012**, *62*, 408–415. [[CrossRef](#)]
5. Myung, S.-T.; Kikuchi, M.; Yoon, C.S.; Yashiro, H.; Sun, Y.-K. A new synthetic method of titanium oxyfluoride and its application as an anode material for rechargeable lithium batteries. *J. Power Sources* **2015**, *288*, 376–383. [[CrossRef](#)]
6. Zhang, Y.; Srot, V.; Moudrakovski, I.; Feng, Y.; van Aken, P.A.; Maier, J.; Yu, Y. Boosting Sodium Storage in TiF₃/Carbon Core/Sheath Nanofibers through an Efficient Mixed-Conducting Network. *Adv. Energy Mater.* **2019**, *9*, 1901470. [[CrossRef](#)]
7. Louvain, N.; Karkar, Z.; El-Ghozzi, M.; Bonnet, P.; Guérin, K.; Willmann, P. Fluorination of anatase TiO₂ towards titanium oxyfluoride TiOF₂: A novel synthesis approach and proof of the Li-insertion mechanism. *J. Mater. Chem. A* **2014**, *2*, 15308–15315. [[CrossRef](#)]
8. Gnedenkov, S.V.; Institute of Chemistry of Far-Eastern Branch of Russian Academy of Sciences; Opra, D.P.; Kuryavyi, V.G.; Sinebryukhov, S.L.; Ustinov, A.Y.; Sergienko, V.I. Nanostructured TiO₂-TiOF₂ composite as anode material for Li-ion battery. *Electrochem. Energetics* **2014**, *14*, 68–77. [[CrossRef](#)]
9. Xu, H.; Wang, W.; Yu, G.; Qin, L.; Jiang, Y.; Ren, L.; Chen, J. Nitrogen-Doped Carbon-Coated TiO₂/TiF₃ Heterostructure Nanoboxes with Enhanced Lithium and Sodium Storage Performance. *ACS Appl. Energy Mater.* **2020**, *3*, 4738–4745. [[CrossRef](#)]
10. Guerin, K.; Louvain, N.; El-Ghozzi, M.; Cenac-Morthe, C. High Performances of Oxyfluoride Electrode Used in Lithium Ion Battery. *E3S Web Conf.* **2017**, *16*, 17007. [[CrossRef](#)]
11. Zhu, J.; Liu, Z.; Yang, F.; Long, D.; Jian, Y.; Pu, S. The Preparation of {001}TiO₂/TiOF₂ via a One-Step Hydrothermal Method and Its Degradation Mechanism of Ammonia Nitrogen. *Materials* **2022**, *15*, 6465. [[CrossRef](#)] [[PubMed](#)]
12. Dwyer, D.B.; Cooke, D.J.; Hidalgo, M.F.; Li, B.; Stanton, J.; Omenya, F.; Bernier, W.E.; Jones, W.E. Fluorine doping of nanostructured TiO₂ using microwave irradiation and polyvinylidene fluoride. *J. Fluor. Chem.* **2019**, *227*, 109375. [[CrossRef](#)]
13. He, M.; Wang, Z.; Yan, X.; Tian, L.; Liu, G.; Chen, X. Hydrogenation effects on the lithium ion battery performance of TiOF₂. *J. Power Sources* **2016**, *306*, 309–316. [[CrossRef](#)]
14. Li, C.; Chen, K.; Zhou, X.; Maier, J. Electrochemically driven conversion reaction in fluoride electrodes for energy storage devices. *npj Comput. Mater.* **2018**, *4*, 22. [[CrossRef](#)]
15. Churikov, A.V.; Ivanishchev, A.V.; Ivanishcheva, I.A.; Zapsis, K.V.; Gamayunova, I.M.; Sycheva, V.O. Kinetics of electrochemical lithium intercalation into thin tungsten (VI) oxide layers. *Russ. J. Electrochem.* **2008**, *44*, 530–542. [[CrossRef](#)]
16. Van der Ven, A.; See, K.A.; Pilon, L. Hysteresis in electrochemical systems. *Batter. Energy* **2022**, *1*, 20210017. [[CrossRef](#)]
17. Ivanishchev, A.V.; Ivanishcheva, I.A. Ion Transport in Lithium Electrochemical Systems: Problems and Solutions. *Russ. J. Electrochem.* **2020**, *56*, 907–928. [[CrossRef](#)]
18. Kulova, T.L.; Skundin, A.M.; Andreev, V.N.; Gryzlov, D.Y.; Mironenko, A.A.; Rudyi, A.S.; Gusev, V.N.; Naumov, V.V. Cyclic voltammetry studies of silicon–aluminum thin-film electrodes synthesized in the presence of oxygen. *Russ. J. Electrochem.* **2015**, *51*, 1157–1161. [[CrossRef](#)]

Disclaimer/Publisher's Note: The statements, opinions and data contained in all publications are solely those of the individual author(s) and contributor(s) and not of MDPI and/or the editor(s). MDPI and/or the editor(s) disclaim responsibility for any injury to people or property resulting from any ideas, methods, instructions or products referred to in the content.